# An improved model considering elastic–plastic contact and partial hydrodynamic lubrication for chemical mechanical polishing

**H-J Tsai**[1], **Y-R Jeng**[2*], and **P-Y Huang**[1]

[1]Department of Mechanical Engineering, WuFeng Institute of Technology, Chia-Yi, Taiwan, Republic of China

[2]Department of Mechanical Engineering, National Chung Cheng University, Chia-Yi, Taiwan, Republic of China

*The manuscript was received on 10 January 2008 and was accepted after revision for publication on 30 May 2008.*

DOI: 10.1243/13506501JET407

**Abstract:** Chemical mechanical polishing (CMP) has become a primary technique for planarization of semiconductor wafers in sub-micro device fabrication. A physical CMP model combines the effects of grain flow hydrodynamic lubrication, pad roughness, and asperity contact between wafer and pad. In this study, an improved CMP model, considering both the grain flow with roughness effects and the micro-contact mechanism, is proposed. The model applies the average lubrication equation with partial hydrodynamic lubrication theory and considers the elastic–plastic micro-contact theory. The applied load acting on the wafer is balanced by the slurry pressure in the non-contact area, and the surface asperity contact force in the contact area. The effects of the CMP parameters including applied load, rotation speed, particle size, and pad roughness are studied and discussed. The simulation results compare well with experimental data in the literature and contribute to further understanding in wafer–pad contact mechanism.

**Keywords:** chemical mechanical polishing, grain flow, roughness, partial hydrodynamic lubrication, elastic–plastic contact, removal rate

## 1 INTRODUCTION

Chemical mechanical polishing (CMP) has been widely used to achieve global planarization of wafers in sub-micro device fabrication [**1**]. Figure 1 shows a schematic diagram of CMP. The wafer is held inside a carrier and pressed onto a rotating polishing pad under a user-defined polishing pressure. During the CMP process, the powder slurry flows between the wafer and polishing pad. The surface of the wafer is polished by a powder slurry flow. Since there are a larger number of operation parameters in the CMP process, the CMP mechanism is inadequately understood. Physically based models are required to provide fundamental insight into the polishing mechanisms.

Preston [**2**] presented the first mechanic model in which the removal rate is related to the pressure and relative velocity between the wafer and the pad. Nanz and Camilletti [**3**] conducted a survey and compared the physical effects of CMP models up to 1995. The published CMP models are mainly based on contact mechanics [**4–8**], slurry hydrodynamics [**9–12**] or lubrication theory [**13**]. Tichy *et al.* [**14**] presented a two-dimensional CMP model including contact mechanics and lubrication hydrodynamics. Thakurta *et al.* [**15**] used lubrication theory to describe lubrication regime (40–70 μm slurry films) and contact regime (thinner films) and accounted for pad compressibility, porosity, and slurry delivery effects. Luo and Dornfeld [**16**] proposed a contact model of the CMP process based on plastic contact over the wafer–abrasive interface and pad–abrasive interface. Liang *et al.* [**17**] investigated the wear behaviour of polishing wafers and pads by comparing different polishing slurries with different additives by real-time CMP experiments. They observed that the polishing removal rate of wafers decreases with decreasing slurry particle size. Lu *et al.* [**18**] used dual emission laser-induced fluorescence to measure slurry thickness and friction

*Corresponding author: Department of Mechanical Engineering, National Chung Cheng University, 160 San-Hsing, Ming-Hsiung, Chia-Yi 621, Taiwan, Republic of China. email: imeyrj@ccu.edu.tw*



Downloaded from pij.sagepub.com at PENNSYLVANIA STATE UNIV on September 17, 2016

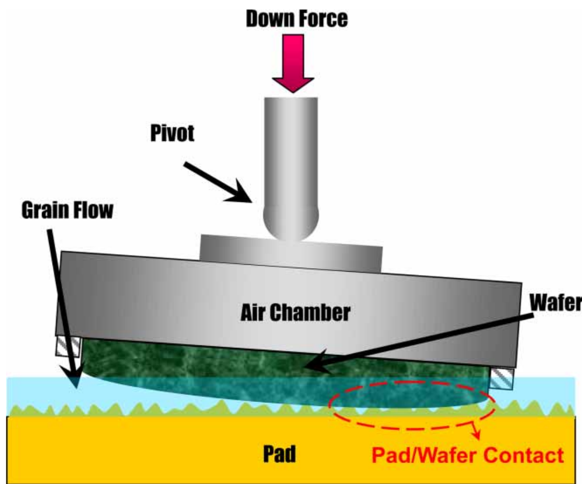


**Fig. 1** Schematic of CMP

force between the wafer and the polishing pad. They demonstrated that both slurry thickness and friction force are dominantly dependent on the shape of the wafer. In previous CMP models, the effects of particle in the slurry and the roughness on the polishing pad surface were almost ignored.

Wornyoh *et al.* [**19**] reviewed the dry particulate lubrication on powder and granular materials. In their paper, the theoretical, experimental, and numerical simulation studies have been reviewed for the behaviour of dry particulate. Iordanoff *et al.* [**20**] described the approaches for modelling the behaviour of third bodies in dry contact. The mathematical modelling of powders falls into two general classes: discrete and continuum models. Elrod [**21**] summarized the theoretical and experimental background of granular flows, giving particular attention to the granular flow theory proposed by Haff [**22**]. In Haff's modelling, the theory of dense gases was adapted to the modelling of grain collisions. A microscopic model was introduced to establish a relationship between the parameters appearing in the conservation laws, and a powerful method was developed for obtaining a physically realistic representation of granular flow from a fluid mechanics perspective. The results from Haff's grain theory were in good agreement with the experiments of Heshmat [**23**] and Dai *et al.* [**24**]. Patir and Cheng [**25**, **26**] developed an average flow model to determine random roughness effects in terms of flow factors. Tripp [**27**] extended the average flow model and generalized a closed form flow factor tensor, which depended on roughness parameters. The flow factor tensor, derived by the Green function technique and using the perturbation approach, has been the most complete description of the interaction between lubricant flow and roughness. The flow factors method has been applied to grain flow lubrication [**28**, **29**].

Yu *et al.* [**30**, **31**] presented a CMP model that combined the polishing pad roughness and slurry hydrodynamic pressure effects. The contact force between polishing pad and wafer was handled using an elastic asperity micro-contact model (G–W model) proposed by Greenwood and Williamson [**32**]. Jeng and Tsai [**33**] proposed a CMP material removal rate model by using Haff's grain theory, hydrodynamic lubrication, and pad roughness. Jeng *et al.* [**34**] used a micro-contact model to investigate the wafer–pad contact pressure. Then, Tsai *et al.* [**35**] proposed an elastopartial hydrodynamic contact model for the CMP process. The model combines the effects of partial hydrodynamic grain flow and elastic micro-contact between wafer and polishing pad. However, the wafer–pad contact was assumed as elastic deformation.

In this paper, an improved model considering asperity contact and grain flow lubrication for the CMP process is proposed. The model combines both the effects of partial hydrodynamic grain flow and elastic-plastic micro-contact between wafer and pad. The grain flow hydrodynamic pressure is analysed using the average flow model. This asperity contact considers the elastic, elastoplastic, and plastic deformations of the polishing pad between wafer and polishing pad. The applied load acting on the wafer is balanced by both the slurry pressure in the non-contact area and the surface asperity contact force in the contact area. The model considers not only the general operating parameters such as applied load and rotation speed but also other important consumable parameters including the polishing pad roughness and particle size. The simulation results, using partial hydrodynamic lubrication and elastic-plastic micro-contact, demonstrate good agreement with the experiments results of Lu *et al.* [**18**] and improves upon current methods for realistic modelling and theoretical understanding of the chemical mechanical polishing mechanisms.

## 2 THEORETICAL MODEL

### 2.1 Partial hydrodynamic lubrication

Haff [**22**] proposed a grain flow theory for the analysis of the behaviour of granular material in motion from a continuum point of view. He treated individual grains as the molecules of a granular fluid. The mean separation ($s$) between neighbouring particles is assumed much less than the particle's diameter ($d$), so bulk density ($\rho$) is treated as constant throughout the gap. In addition to bulk flow velocity ($u$), each particle is free to move within its cell at an average fluctuation velocity ($v$), which is commonly referred to as the granular pseudo-temperature. Due to particle collision using microscopic kinetic models, the expressions for the



Downloaded from pij.sagepub.com at PENNSYLVANIA STATE UNIV on September 17, 2016

pressure ($p$), viscosity ($\eta$), thermal diffusivity ($K$) and energy loss ($I$) are described as follows

$$p = td\rho\frac{v^2}{s}; \quad \eta = ad^2\rho\frac{v}{s}; \; K = kd^2\frac{v}{s}; \; I = w\rho\frac{v^3}{s} \tag{1}$$

where the coefficients $t$, $a$, and $k$ are dimensionless constants; for $w = 1 - e^2$ and $e$ is the coefficient of restitution.

The continuity, momentum and energy equations are described as follows:

*The continuity equation*

$$\frac{\partial\rho}{\partial t} + \frac{\partial}{\partial x_i}(\rho u_i) = 0 \tag{2}$$

*The momentum equation*

$$\frac{\partial}{\partial t}(\rho u_i) + \frac{\partial}{\partial x_k}\left[p\delta_{ik} + \rho u_i u_k - \eta\left(\frac{\partial u_i}{\partial x_k} + \frac{\partial u_k}{\partial x_i}\right)\right] - \rho g_i = 0 \tag{3}$$

*The energy equation*

$$\frac{\partial}{\partial t}\left(\frac{1}{2}\rho u^2 + \frac{1}{2}\rho v^2\right) = -\frac{\partial}{\partial x_k}\left[\rho u_k\left(\frac{p}{\rho} + \frac{1}{2}u^2 + \frac{1}{2}v^2\right) - U_i\eta\left(\frac{\partial u_i}{\partial x_k} + \frac{\partial u_k}{\partial x_i}\right) - K\frac{\partial}{\partial x_k}\left(\frac{1}{2}\rho v^2\right)\right] + \rho u_i g_i - I \tag{4}$$

Figure 1 illustrates a schematic of the CMP process. The wafer and pad are considered to be equal in width. Based on order-of-magnitude analysis, Haff's grain flow theory and using the Patir/Cheng flow factors by Tripp's perturbation approach, the generalized average lubrication equation is obtained as [**28**]

$$\partial_i\left(\frac{1}{6}\frac{t}{a}\cdot B\cdot\Psi\cdot\overline{h}^2\cdot\overline{\Phi}^{\mathrm{P}}_{ij}\cdot\partial_i(\overline{\ln p})\right) = -V_j\cdot\partial_i\left(Z\cdot\delta_{ij} + \frac{1}{2}\cdot\sigma\cdot\overline{\Phi}^{\mathrm{S}}_{ij}\right) \tag{5}$$

where

$$\Psi = \Psi_{\mathrm{ine}}\left(H_{\mathrm{P}}, \frac{w}{k}\right) = \sqrt{\frac{k}{w}}\cdot\frac{R_2 - 2}{R_1} \tag{6}$$

$$R_1(x, y) = \exp\left(\sqrt{\frac{w}{k}}\frac{h}{d}\right) - \exp\left(-\sqrt{\frac{w}{k}}\frac{h}{d}\right)$$

$$R_2(x, y) = \exp\left(\sqrt{\frac{w}{k}}\frac{h}{d}\right) + \exp\left(-\sqrt{\frac{w}{k}}\frac{h}{d}\right) \tag{7}$$

where $\overline{\Phi}^{\mathrm{P}}_{ij}$, $\overline{\Phi}^{\mathrm{S}}_{ij}$ are pressure and shear flow factor tensors, respectively.

The results of flow factors are derived and expressed as functions of Peklenik number, the standard deviation of the roughness height of each surface, the film thickness ratio ($H_{\mathrm{S}} = \overline{h}/\sigma$), and the film particle ratio (defined as $H_{\mathrm{P}} = \overline{h}/d$). The flow factors are obtained as

$$\overline{\Phi}^{\mathrm{P}}_{xx} = 1 + \left(\frac{\sigma}{\overline{h}}\right)^2\cdot g(H_{\mathrm{P}})\cdot\left\{1 - \frac{[f(H_{\mathrm{P}})]^2}{g(H_{\mathrm{P}})}\cdot\left[\left(\frac{\sigma_2}{\sigma}\right)^2\Omega_2 + \left(\frac{\sigma_1}{\sigma}\right)^2\Omega_1\right]\right\} \tag{8}$$

$$\overline{\Phi}^{\mathrm{P}}_{xy} = \overline{\Phi}^{\mathrm{P}}_{yx} = -\left(\frac{\sigma}{\overline{h}}\right)^2\cdot f^2(H_{\mathrm{P}})\cdot\left[\left(\frac{\sigma_2}{\sigma}\right)^2\Psi_2 + \left(\frac{\sigma_1}{\sigma}\right)^2\Psi_1\right] \tag{9}$$

$$\overline{\Phi}^{\mathrm{P}}_{yy}(\theta_1, \theta_2) = \overline{\Phi}^{\mathrm{P}}_{xx}(90^\circ - \theta_1,\, 90^\circ - \theta_2) \tag{10}$$

$$\overline{\Phi}^{\mathrm{S}}_{xx} = -\left(\frac{\sigma}{\overline{h}}\right)\cdot f(H_{\mathrm{P}})\cdot\left[\left(\frac{\sigma_2}{\sigma}\right)^2\Omega_2 - \left(\frac{\sigma_1}{\sigma}\right)^2\Omega_1\right] \tag{11}$$

$$\overline{\Phi}^{\mathrm{S}}_{xy} = \overline{\Phi}^{\mathrm{S}}_{yx} = -\left(\frac{\sigma}{\overline{h}}\right)\cdot f(H_{\mathrm{P}})\cdot\left[\left(\frac{\sigma_2}{\sigma}\right)^2\Psi_2 - \left(\frac{\sigma_1}{\sigma}\right)^2\Psi_1\right] \tag{12}$$

$$\overline{\Phi}^{\mathrm{S}}_{yy}(\theta_1, \theta_2) = \overline{\Phi}^{\mathrm{S}}_{xx}(90^\circ - \theta_1,\, 90^\circ - \theta_2) \tag{13}$$

$$\overline{\Phi}_{fs} = -3\left(\frac{\sigma}{\overline{h}}\right)^2\cdot\left[\left(\frac{\sigma_2}{\sigma}\right)^2\Psi_2 - \left(\frac{\sigma_1}{\sigma}\right)^2\Psi_1\right] \tag{14}$$

$$\overline{\Phi}_{fp} = 1 - \left(\frac{\sigma}{\overline{h}}\right)^2\cdot f(H_{\mathrm{P}})\cdot\left[\left(\frac{\sigma_2}{\sigma}\right)^2\Psi_2 + \left(\frac{\sigma_1}{\sigma}\right)^2\Psi_1\right] \tag{15}$$

where $\Omega_i$ and $\Psi_i$ are orientation coefficients of the $i$th surface while $f(H_{\mathrm{P}})$ and $g(H_{\mathrm{P}})$ are grain size coefficients, as follows

$$\Omega_i = \cos^2\theta_i\cdot\frac{1}{\gamma_i + 1} + \sin^2\theta_i\cdot\frac{\gamma_i}{\gamma_i + 1} \tag{16}$$

$$\Psi_i = \sin\theta_i\cdot\cos\theta_i\cdot\frac{1 - \gamma_i}{\gamma_i + 1} \tag{17}$$

$$f(H_{\mathrm{P}}) = 2 + \sqrt{\frac{w}{k}}\cdot\frac{h}{d}\cdot\left(\frac{R_1}{R_2 - 2} - \frac{R_2}{R_1}\right) \tag{18}$$

$$g(H_{\mathrm{P}}) = 1 + 2\sqrt{\frac{w}{k}}\cdot\frac{\overline{h}}{d}\cdot\left(\frac{R_1}{R_2 - 2} - \frac{R_2}{R_1}\right) + \frac{w}{k}\cdot\left(\frac{\overline{h}}{d}\right)^2\cdot\left[\left(\frac{R_2}{R_1}\right)^2 - \frac{R_2 - 1}{R_2 - 2}\right] \tag{19}$$

where $\theta_i$ is the roughness orientation angle of the $i$th surface, $\sigma$ defined as $\sigma = \sqrt{\sigma_1^2 + \sigma_2^2}$ represents the



Downloaded from pij.sagepub.com at PENNSYLVANIA STATE UNIV on September 17, 2016

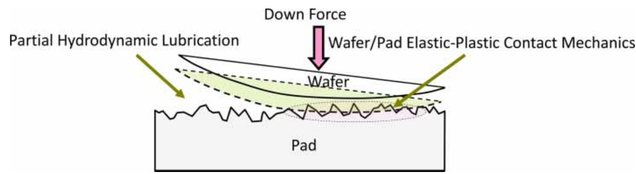


**Fig. 2** The variation of the wafer–pad polishing interface when the down force acts on the wafer

standard deviation of combined roughness $\delta$, and $\sigma_i$ the standard deviation of $\delta_i$, where subscripts 1 and 2 represent pad and wafer surfaces, respectively.

### 2.2 The micro-contact model

Besides the partial hydrodynamic lubrication, the wafer–pad asperity contact also plays an important role in CMP. The contact conditions for wafer and polishing pad are determined by clearance, shown in Fig. 2. The elastic, elastoplastic, and plastic deformations of the polishing pad may be produced during the CMP process. The contact between wafer and pad is assumed as elastic deformation in an earlier paper [**35**]. In this paper, the wafer–pad contact area was calculated using a micro-contact model that considered the elastic, elastoplastic, and plastic deformations of the polishing pad [**32**, **36–38**]. If the clearance is less than $3R_q$, where $R_q$ is the root mean square of the pad asperity heights, the wafer–pad interface area is considered in contact [**30**]. Greenwood and Williamson [**32**] proposed the classical statistical asperity micro-contact model (*G–W* model) to describe the elastic contact phenomena between two surfaces. In the *G–W* model, the deformation for each asperity in contact is governed by the Hertzian micro-contacts. The contact pressure and the real area of contact between wafer and pad can be described as follows

$$\frac{F_e}{A_n \cdot E'} = \frac{4}{3} \cdot \eta_a \cdot R^{1/2} \cdot \int_D^{D+\omega} (z-D)^{3/2} \cdot \varphi(z)\mathrm{d}z \tag{20}$$

$$\frac{A_e}{A_n} = \eta_a \cdot \pi \cdot R \cdot \int_D^{\infty} (z-D) \cdot \varphi(z)\mathrm{d}z \tag{21}$$

where $A_n$ is the nominal area of contact between pad and wafer, $\eta_a$ is the area density of asperities on pad surface, $R$ is the average radius of asperity curvatures on pad surface, $z$ and $D$ are the asperity height and surface separation, respectively, measured from a reference plane placed at the asperity mean height, the interference $\omega$ is defined as $z-D$, and $\varphi(z)$ is the distribution function of the asperity heights, and $E'$ is the equivalent Young's modulus between the wafer and the pad

$$\frac{1}{E'} = \frac{1-\nu_1^2}{E_1} + \frac{1-\nu_2^2}{E_2} \tag{22}$$

However, asperities could deform plastically when the applied load exceeds about half of the yield point load. Abbott and Firestone [**39**] developed the most widely used model for a fully plastic contact, i.e. surface micro-geometry model. The contact pressure and real area of the contact for plastically deformed asperities can be expressed as follows

$$\frac{F_p}{A_n \cdot E'} = 2 \cdot \pi \cdot \eta_a \cdot R \cdot \frac{H}{E'} \cdot \int_{D+\omega_p}^{\infty} (z-D) \cdot \varphi(z)\,\mathrm{d}z \tag{23}$$

$$\frac{A_p}{A_n} = 2 \cdot \eta_a \cdot \pi \cdot R \cdot \int_{D+\omega_p}^{\infty} (z-D) \cdot \varphi(z)\,\mathrm{d}z \tag{24}$$

where $H$ is the pad hardness and $\omega_p$ is the critical interference at the point of a fully plastic flow. Jeng and Wang [**36**] extended the elastoplastic micro-contact model proposed by Zhao *et al.* [**37**] to the elliptical contact of surface asperities by applying the concept of volume conservation to the plastic deformation of asperities during the elastoplastic and plastic stage. The transition from elastic deformation to fully plastic flow of asperity is present based on contact mechanics theories in conjunction with the continuity and smoothness of variables across different modes of deformation. The elastoplastic contact pressure and real area of contact are as follows

$$\frac{F_{ep}}{A_n \cdot E'} = \eta_a \cdot \pi \cdot R \cdot \frac{H}{E'} \cdot \int_{D+\omega_e}^{D+\omega_p} \left[1 - 1\left(1 - k\frac{\ln\omega_p - \ln\omega}{\ln\omega_p - \ln\omega_e}\right)\right] \cdot \left[1 - 2\left(\frac{\omega-\omega_e}{\omega_p-\omega_e}\right)^3 + 3\left(\frac{\omega-\omega_e}{\omega_p-\omega_e}\right)^2\right] \cdot (z-D) \cdot \varphi(z)\,\mathrm{d}z \tag{25}$$

$$\frac{A_{ep}}{A_n} = \eta_a \cdot \pi \cdot R \cdot \int_{D+\omega_e}^{D+\omega_p} [z-D] \cdot \left[1 - 2\left(\frac{\omega-\omega_e}{\omega_p-\omega_e}\right)^3 + 3\left(\frac{\omega-\omega_e}{\omega_p-\omega_e}\right)^2\right] \cdot (z-D) \cdot \varphi(z)\,\mathrm{d}z \tag{26}$$

where $\omega_e$ is the critical interference at the point of initial yield and can be determined as follows

$$\omega_e = \left(\frac{3\pi kH}{4E'}\right)^2 R \tag{27}$$

Based on the effort by Johnson [**40**], the minimum value of critical contact interference ($\omega_p$) in the fully plastic deformation would be at least 54 times that at initial yielding (i.e. $\omega_p = 54\omega_e$). When $\omega < \omega_e$, the contact is elastic. When $\omega \geqslant \omega_p$, a complete plastic deformation occurs. When $\omega_e \leqslant \omega \leqslant \omega_p$, the asperity deforms elastoplastically. The total contact pressure

 JET407 © IMechE 2008

Downloaded from pij.sagepub.com at PENNSYLVANIA STATE UNIV on September 17, 2016

and the real area of contact for wafer–pad surfaces are expressed as follows

$$\frac{F_{\text{total}}}{A_{\text{n}} \cdot E'} = \frac{F_{\text{e}}}{A_{\text{n}} \cdot E'} + \frac{F_{\text{ep}}}{A_{\text{n}} \cdot E'} + \frac{F_{\text{p}}}{A_{\text{n}} \cdot E'} = \frac{4}{3} \cdot \eta_{\text{a}} \cdot R^{1/2} \cdot \int_{D}^{D+\omega} (z-D)^{3/2} \cdot \varphi(z)\text{d}z + \eta_{\text{a}} \cdot \pi \cdot \frac{H}{E'} \cdot \int_{D+\omega_{\text{e}}}^{D+\omega_{\text{p}}} \left[1 - 1\left((1-k) \cdot \frac{\ln \omega_{\text{p}} - \ln \omega - \ln 2}{\ln \omega_{\text{p}} - \ln \omega_{\text{e}}}\right)\right] \cdot \left[1 - 2\left(\frac{\omega - \omega_{\text{e}}}{\omega_{\text{p}} - \omega_{\text{e}}}\right)^3 + 3\left(\frac{\omega - \omega_{\text{e}}}{\omega_{\text{p}} - \omega_{\text{e}}}\right)^2\right] \cdot (z-D) \cdot \varphi(z)\text{d}z + 2 \cdot \pi \cdot \eta_{\text{a}} \cdot R \cdot \frac{H}{E'} \cdot \int_{D+\omega_{\text{p}}}^{\infty} (z-D) \cdot \varphi(z)\text{d}z \tag{28}$$

$$\frac{A_{\text{r}}}{A_{\text{n}}} = \eta_{\text{a}} \cdot \pi \cdot R \cdot \int_{D}^{D+\omega_{\text{e}}} (z-D) \cdot \varphi(z)\text{d}z + 2 \cdot \eta_{\text{a}} \cdot \pi \cdot R \cdot \int_{D+\omega_{\text{p}}}^{\infty} (z-D) \cdot \varphi(z)\text{d}z + \eta_{\text{a}} \cdot \pi \cdot R \cdot \int_{D+\omega_{\text{e}}}^{D+\omega_{p}} (z-D) \cdot \left[1 - 2\left(\frac{\omega - \omega_{\text{e}}}{\omega_{\text{p}} - \omega_{\text{e}}}\right)^3 + 3\left(\frac{\omega - \omega_{\text{e}}}{\omega_{\text{p}} - \omega_{\text{e}}}\right)^2\right] \cdot \varphi(z)\text{d}z \tag{29}$$

## 3 SIMULATION AND DISCUSSION

### 3.1 Wafer–pad geometry

The calculated slurry film thickness ($\overline{h}$) represents average slurry film thickness at the center of the wafer O. The wafer is assumed to have a convex curvature, as in Runnels and Eyman [**9**] and Thakurta *et al.* [**15**]. The dome height ($\delta_{\text{d}}$) represents displacement distance at wafer center of the curved wafer wall past its natural uncurved border. The average slurry film thickness $\overline{h}$ can be calculated by wafer curvature radius ($R_{\text{c}}$), wafer radius ($R_{\text{W}}$), dome height ($\delta_{\text{d}}$), attack angle ($\theta$), mean surface height between wafer center, and pad ($h_0$), and the distance from wafer center ($x_{\text{W}}$) as follows [**41**]

$$\overline{h} = h_0 + (R_{\text{c}} - \delta_{\text{d}})\cos\theta - \sqrt{[(R_{\text{c}} - \delta_{\text{d}})\cos\theta + x_{\text{W}}\sin\theta]^2 + R_{\text{W}}^2 - x_{\text{W}}^2} \tag{30}$$

where the coordinate origin is located at the center of the wafer. Table 1 summarizes the ranges and base case values of the parameters and grain conditions used in this simulation. The simulation conditions are the same as in reference [**18**]. The particles were on the order of 100–200 nm in the experiments of Lu *et al.* [**18**]. They used Freudenberg FX-9 polishing pads with asperities on the order of 10–20 μm. Grain conditions are according to the order of magnitude analysis as in Dai *et al.* [**24**] (i.e. $t/a = 1$, $k/w = 4 \times 10^{-6}$, $v/u = 3$). The Peklenik number is simplified as isotropic (i.e. $\gamma = 1$). The wafer surface is assumed smooth and less than the pad surface ($\sigma_2 \ll \sigma_1$). In the following, $\sigma$ is equivalent to $\sigma_1$.

**Table 1** The range of input parameters and grain conditions in the CMP process

| Parameters and grain conditions | Range | Base case |
|---|---|---|
| Wafer diameter (in) | | 3 |
| Applied load (psi) | 2–6 | 4 |
| Relation rotation speed (r/min) | 30–90 | 60 |
| Dome height (μm) | | 5 |
| Pad roughness (μm) | 10, 20 | 15 |
| Particle diameter (nm) | 100, 200 | 100 |
| $t/a$ | | 1 |
| $w/k$ | | 0.000 004 |
| $V/U$ | | 3 |

### 3.2 Comparison with experiment results

The following simulation calculates slurry film thickness considering both the force and momentum equilibria. The applied pressure ($P_{\text{applied}}$) is the sum of the partial hydrodynamic pressure ($P_{\text{fluid}}$) and the wafer–pad asperity contact pressure ($P_{\text{con}}$). The pressure relation is expressed as

$$P_{\text{applied}} = P_{\text{fluid}} + P_{\text{con}} \tag{31}$$

Two types of theoretical results including hydrodynamic lubrication and asperity contact are used.

1. Hydrodynamic lubrication analysis: pad roughnesses, $\sigma = 20$ and 10 μm.
2. Hydrodynamic lubrication and elastic–plastic micro-contact (LEP): the elastic, elastoplastic, and plastic deformations of polishing pad are considered.

The pad roughness is selected as $\sigma = 15$ μm. The hydrodynamic lubrication analysis neglects the micro-contact and only considers the partial hydrodynamic lubrication. However, the LEP analysis simultaneously considers micro-contact and partial hydrodynamic lubrication. The theoretical results are first compared with the experiment data of Lu *et al.* [**18**]. The values of film thickness, attack angle, contact area ratio, and varying relative removal rate with applied load and rotation speed for various particle sizes are investigated.

Dome height, $\delta_{\text{d}} = 5$ μm, and particle size, $d = 100$ nm were selected (Figs 3 and 4). Figure 3 shows that as the applied load increase the slurry film thickness



Downloaded from pij.sagepub.com at PENNSYLVANIA STATE UNIV on September 17, 2016

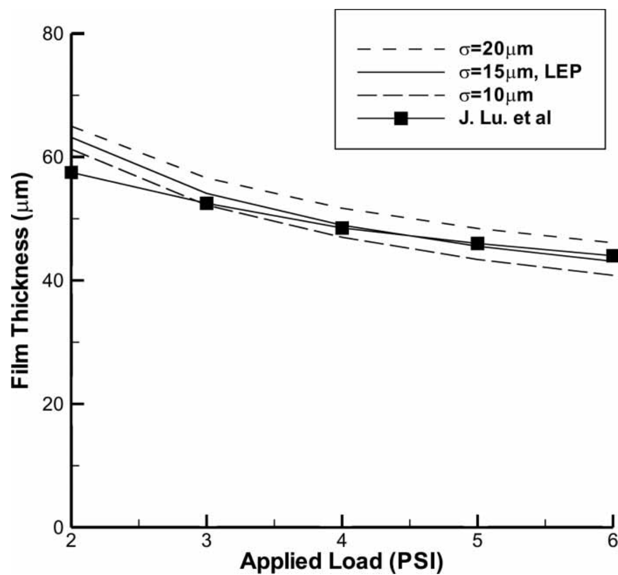


**Fig. 3** Comparison of predicted film thickness ($\sigma = 20\,\mu m$, $15\,\mu m$ LEP, and $10\,\mu m$) with experimental data at various applied loads

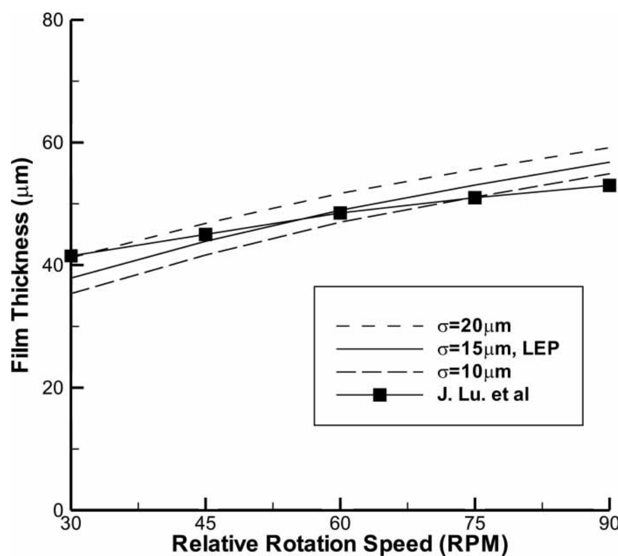


**Fig. 4** Comparison of predicted film thickness ($\sigma = 20\,\mu m$, $15\,\mu m$ LEP, and $10\,\mu m$) with experimental data at various relative speeds

decreases. The slurry film thickness of the theoretical results ($\sigma = 20, 10$, and $15\,\mu m$ (LEP)) in this work is approximately the film thickness measured by Lu *et al.* [**18**]. Figure 4 shows the slurry film thickness increases with increasing rotation speed. The slurry film thickness of our theoretical results is also approximately the film thickness measured by Lu *et al.* [**18**]. The LEP analysis ($\sigma = 15\,\mu m$) shows good agreement with experiment data.

As applied load increases, it is obvious that the LEP analysis ($\sigma = 15\,\mu m$) shows good agreement with the experiment of Lu *et al.* [**18**], as shown in Fig. 3. That is, the asperity deformation becomes significant at high load. Furthermore, the applied load has more pronounced influence on the asperity deformation than rotation speed does in Figs 3 and 4. Results shown in Figs 3 and 4 conclude that the theoretical LEP analysis (includes pad asperity and partial hydrodynamic lubrication) of the CMP process agree well with the experimental results [**41**] and are thus extended to the following parameter studies.

### 3.3 Parameter study

The slurry film thickness, attack angle, contact area ratio, and removal rate are investigated under variation of applied load and rotation speed for $\sigma = 15\,\mu m$ (LEP). Two different particle sizes are compared: 100 and 200 nm. As shown in Fig. 5, the slurry film thickness at a fixed applied load increases with increasing particle size. The attack angle (i.e. wafer tilt angle) creates converging grain flow and provides hydrodynamic load. The attack angle decreases lightly as the applied load increases, and larger particle sizes have higher attack angle at any given load. Figure 6 shows the increase in slurry film thickness at relative rotation speed with increasing particle size. The attack angle increases lightly with increasing relative rotation speed. Similarly, larger particle size have higher film thickness and attack angle at the fixed relative rotation speed.

To investigate the relationship between particle size and pad roughness on contact area ratios and removal rate, three types are selected as follows: (a) $d = 100\,nm$, $\sigma = 15\,\mu m$; (b) $d = 100\,nm$, $\sigma = 20\,\mu m$; (c) $d = 200\,nm$, $\sigma = 20\,\mu m$. The contact area ratio can be defined as: (area of contact portion)/(area of

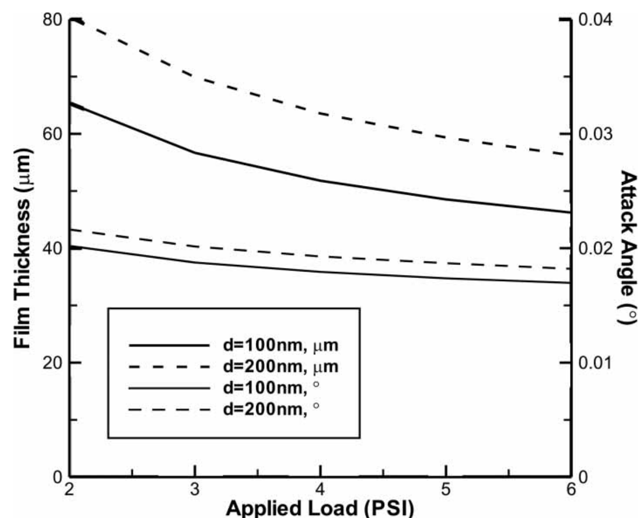


**Fig. 5** Variation of film thickness and attack angle with applied load at different particle size



Downloaded from pij.sagepub.com at PENNSYLVANIA STATE UNIV on September 17, 2016

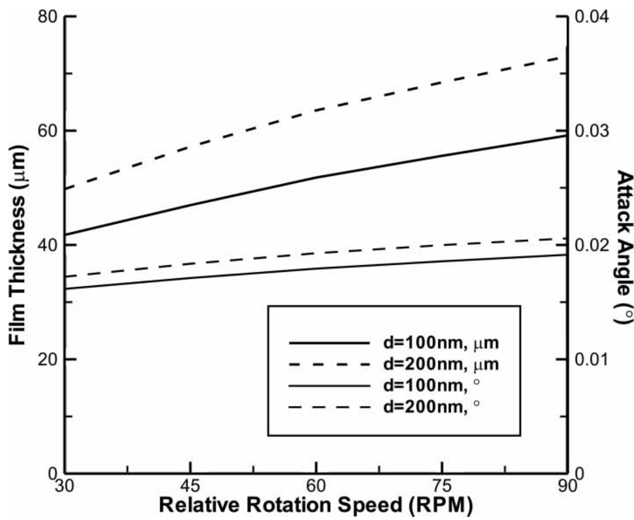


**Fig. 6** Variation of film thickness and attack angle with relative rotation speeds at different particle size

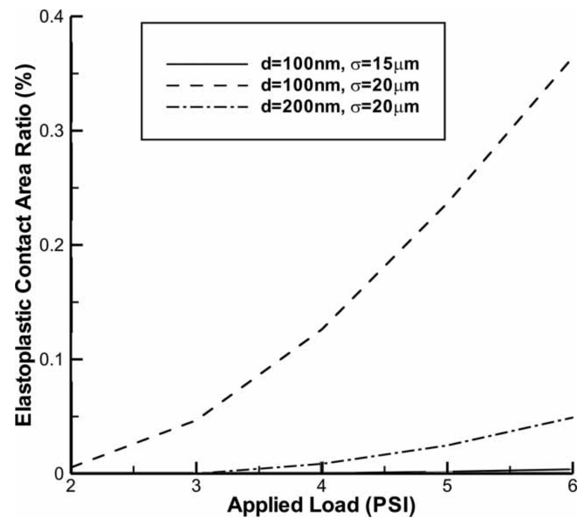


**Fig. 8** Variation of elastoplastic contact area ratio with applied load at different particle size and pad roughness

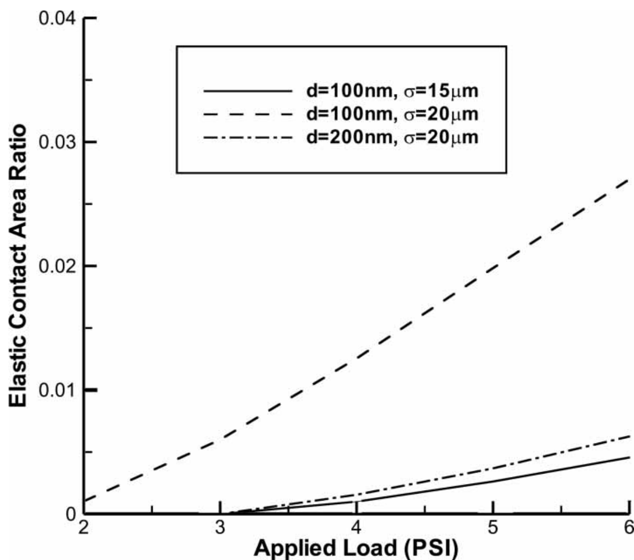


**Fig. 7** Variation of elastic contact area ratio with applied load at different particle size and pad roughness

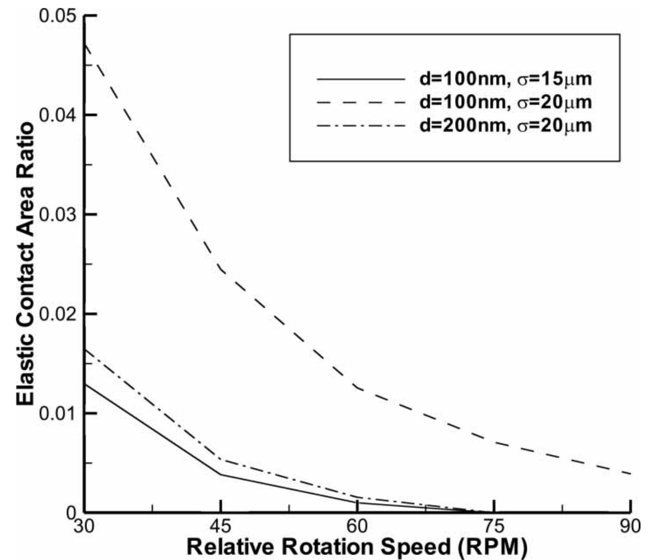


**Fig. 9** Variation of elastic contact area ratio with relative rotation speeds at different particle size and pad roughness

the interface). Figures 7 to 10 show the variation of elastic contact area ratios and elastoplastic contact area ratios under various applied loads/relative rotation speeds. In Fig. 7, the elastic contact area ratio increases as applied loads increases. In Fig. 8, the elastoplastic contact area ratio increases lightly as the applied load increases. Smaller particle size and larger pad roughness has higher elastic–elastoplastic contact area ratios due to its lower film thickness ratio.

In Fig. 9, the elastic contact area ratio decreases as relative rotation speed increases. The results show that lower relative rotation speed lead to increase elastic contact ratio. In Fig. 10, the elastoplastic contact area ratio also decreases as the relative rotation speed increase. In Figs 7 to 10, the elastic–elastoplastic contact area ratios are quantitatively calculated and increase the microscopic understanding of CMP process.

Finally, the effects of particle size and pad roughness under various applied loads and rotational speeds on removal rate are investigated. The removal rate equation, proposed by Runnels and Eyman [**9**], is used: $RR = K\sigma_n\tau$ where $\sigma_n$ is the normal stress, $\tau$ the shear stress, and $K$ the Preston coefficient. The proposed model predicts the removal rate incorporating asperity contact (elastic–elastoplastic contact) and powder



Downloaded from pij.sagepub.com at PENNSYLVANIA STATE UNIV on September 17, 2016

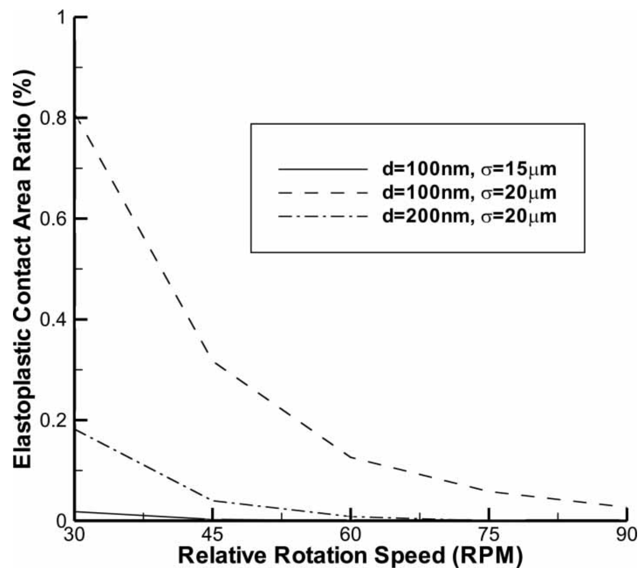


**Fig. 10** Variation of elastoplastic contact area ratio with relative rotation speeds at different particle size and pad roughness

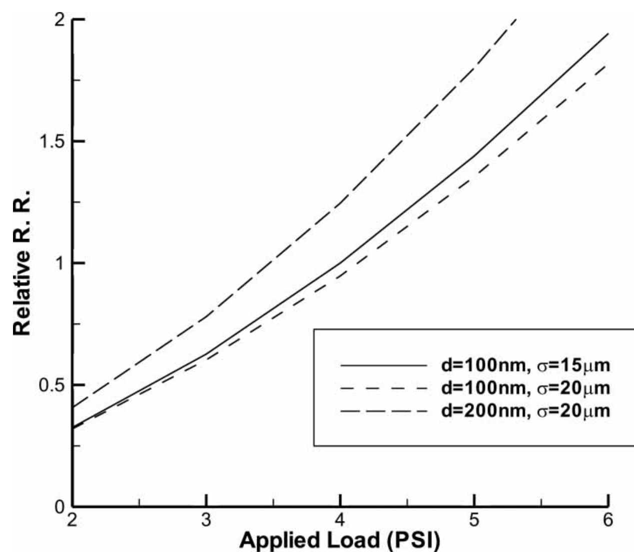


**Fig. 11** Predicted relative removal rate with applied load at different particle size and pad roughness

slurry hydrodynamic lubrication between wafer and rough pad. Figures 11 and 12 demonstrate the relative removal rates; the curves are normalized relative to a particle diameter ($d = 100$ nm) and a pad roughness ($\sigma = 15\,\mu$m). The removal rate increases with increasing applied load and rotational speed. Comparing the results, shown in Figs 11 and 12, the applied load has a larger influence than rotational speed does, on removal rate. The results also show that larger particle size has a higher removal rate at any given load/rotational speed. The removal rate decreases when the pad roughness increases.

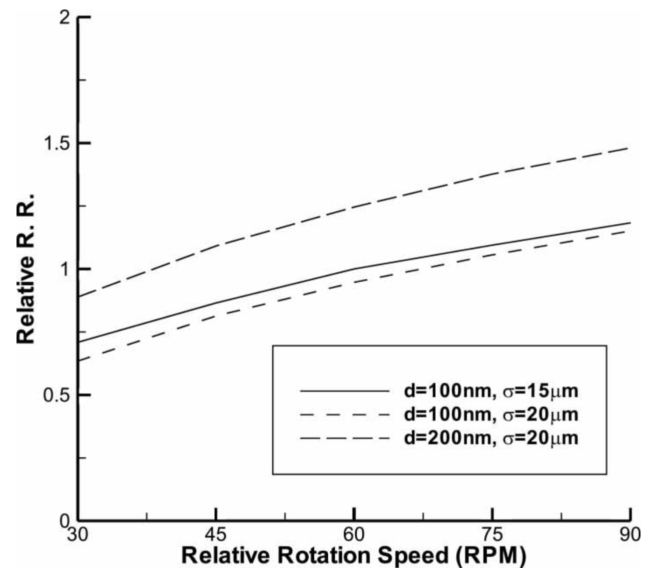


**Fig. 12** Predicted relative removal rate with relative rotation speeds at different particle size and pad roughness

## 4 CONCLUSIONS

In this study, an improved CMP model considering the partial hydrodynamic grain flow lubrication and elastic–plastic micro-contact theory is presented. The predicted results compare well with the experimental observations found in the literature. Pad roughness and particle size effects on the elastic–elastoplastic contact area ratios and the removal rate are discussed. The contact area ratios, which include elastic and elastoplastic contacts, are quantitatively demonstrated. The proposed model, using elastic–plastic micro-contact and partial hydrodynamic lubrication theory, improves upon current methods for realistic modelling and theoretical understanding of chemical mechanical polishing mechanisms.

## ACKNOWLEDGEMENT

The authors gratefully acknowledge the support by the National Science Council of Taiwan under Grant no. NSC 94-2212-E-274-002.

## REFERENCES

1 **Luo, J.** and **Dornfeld, D. A.** *Integrated modeling of chemical mechanical planarization for sub-micron IC fabrication*, 2004 (Springer, Berlin, Germany).
2 **Preston, F. W.** The theory and design of plate glass polishing machines. *J. Soc. Glass Technol.*, 1927, **11**, 214–256.
3 **Nanz, G.** and **Camilletti, L. E.** Modeling of chemical-mechanical polishing: a review. *IEEE Trans. Semi. Manuf.*, 1995, **8**, 382–389.



Downloaded from pij.sagepub.com at PENNSYLVANIA STATE UNIV on September 17, 2016

4 **Bhushan, M., Rouse, R.,** and **Lukens, J. E.** Chemical mechanical polishing in semidirect contact mode. *J. Electrochem. Soc.*, 1995, **142**, 3845–3851.
5 **Srinivasa-Murthy, C., Wang, D., Beaudoin, S. P., Bibby, T., Holland, K.,** and **Cale, T. S.** Stress distribution in chemical mechanical polishing. *Thin Solid Films*, 1997, **308–309**, 533–537.
6 **Chekina, O. G., Keer, L. M.,** and **Liang, H.** Wear-contact problems and modeling of chemical mechanical polishing. *J. Electrochem. Soc.*, 1998, **145**, 2100–2106.
7 **Tseng, W., Wang, Y.,** and **Chin, J.** Effects of film stress on the chemical mechanical polishing process. *J. Electrochem. Soc.*, 1999, **146**, 4273–4280.
8 **Zhao, Y.** and **Chang, L.** A micro-contact and wear model for chemical–mechanical polishing of silicon wafers. *Wear*, 2002, **252**, 220–226.
9 **Runnels, S. R.** and **Eyman, L. M.** Tribology analysis of chemical-mechanical polishing. *J. Electrochem. Soc.*, 1994, **141**, 1698–1701.
10 **Runnels, S. R.** Feature-scale fluid-based erosion modeling for chemical-mechanical polishing. *J. Electrochem. Soc.*, 1994, **141**, 1900–1904.
11 **Rogers, C., Coppeta, J., Racz, L., Philipossian, A., Kaufman, F. B.,** and **Bramono, D.** Analysis of flow between a wafer and pad during CMP process. *J. Electron Mater.*, 1998, **27**, 1082–1087.
12 **Chen, J. M.** and **Fang, Y. C.** Hydrodynamic characters of the thin film fluid in chemical-mechanical polishing. *IEEE Trans. Semi. Manuf.*, 2002, **15**, 39–44.
13 **Sundararajan, S., Thakurta, D. G., Schwendeman, D. W., Murarka, S. P.,** and **Gill, W. N.** Two-dimensional wafer-scale chemical mechanical planarization models based on lubrication theory and mass transport. *J. Electrochem. Soc.*, 1999, **146**, 761–766.
14 **Tichy, J., Levert, J. A., Shan, L.,** and **Danyluk, S.** Contact mechanics and lubrication hydrodynamics of chemical mechanical polishing. *J. Electrochem. Soc.*, 1999, **146**, 1523–1528.
15 **Thakurta, D. G., Borst, C. L., Schwendeman, D. W., Gutmann, R. J.,** and **Gill, W. N.** Pad porosity, compressibility and slurry delivery effects in chemical-mechanical planarization: modeling and experiments. *Thin Solid Films*, 2000, **336**, 181–190.
16 **Luo, J.** and **Dornfeld, D. A.** Material removal mechanism in chemical mechanical polishing: theory and modeling. *IEEE Trans. Semi. Manuf.*, 2001, **14**, 112–133.
17 **Liang, H., Kaufman, F., Sevilla, R.,** and **Aniur, S.** Wear phenomena in chemical mechanical polishing. *Wear*, 1997, **211**, 271–279.
18 **Lu, J., Coppeta, J., Rogers, C., Racz, L., Philipossian, A., Moinpour, M.,** and **Kaufman, F.** The effect of wafer shape on slurry film thickness and friction coefficients in chemical mechanical planarization. In Proceedings of the Materials Research Society Symposium, San Francisco, 2000, vol. 613, E1.2.1.
19 **Wornyoh, E. Y. A., Jasti, V. K.,** and **Higgs III, C. F.** A review of dry particulate lubrication: powder and granular materials. *ASME J. Tribol.*, 2007, **129**, 438–449.
20 **Iordanoff, I., Berthier, Y., Descartes, S.,** and **Heshmat, H.** A review of recent approaches for modeling solid third bodies. *ASME J. Tribol.*, 2002, **124**, 725–735.
21 **Elrod, H. G.** Granular flow as a tribological mechanism – a first look. In Proceedings of the Leeds–Lyon Symposium, Interface Dynamics, BHRA, 1988, pp. 75–102.
22 **Haff, P. K.** Grain flow as a fluid-mechanical phenomenon. *J. Fluid Mech.*, 1983, **134**, 401–430.
23 **Heshmat, H.** The quasi-hydrodynamic mechanism of powder lubrication. Part 2: lubricant film pressure profile. *Lubr. Eng.*, 1992, **48**, 373–383.
24 **Dai, F., Khonsari, M. M.,** and **Lu, Y. Z.** On the lubrication mechanism of grain flows. *Tribol. Trans.*, 1994, **37**, 516–524.
25 **Patir, N.** and **Cheng, H. S.** An average flow model for determining effects of three-dimensional roughness of partial hydrodynamic lubrication. *Trans. ASME, J. Lubr. Technol.*, 1978, **100**, 12–17.
26 **Patir, N.** and **Cheng, H. S.** Application of average flow model to lubrication between rough sliding surfaces. *Trans. ASME, J. Lubr. Technol.*, 1979, **101**, 220–230.
27 **Tripp, J. H.** Surface roughness effects in hydrodynamic lubrication: the flow factor method. *Trans. ASME, J. Lubr. Technol.*, 1983, **105**, 458–465.
28 **Tsai, H. J.** and **Jeng, Y. R.** An average lubrication equation for thin film grain flow with surface roughness effects. *Trans. ASME, J. Tribol.*, 2002, **124**, 736–742.
29 **Jeng, Y. R.** and **Tsai, H. J.** Grain flow lubrication of finite width slider bearings with rough surfaces. *Tribol. Lett.*, 2002, **13**, 219–232.
30 **Yu, T. K., Yu, C. C.,** and **Oriowski, M.** A statistical polishing pad model for chemical-mechanical polishing. In Proceedings of the IEEE International Electron Devices Meeting, Washington, DC, 1993, pp. 865–868.
31 **Yu, T. K., Yu, C. C.,** and **Oriowski, M.** Combined asperity contact and fluid flow model for chemical-mechanical polishing. In the IEEE International Workshop on Numerical Modeling of Processes and Devices for Integrated Circuits, New York, 1994, pp. 29–32.
32 **Greenwood, J. A.** and **Williamson, J. B. P.** Contact of nominal flat surface. *Proc. R. Soc. London, Ser. A.*, 1996, **A295**, 300–319.
33 **Jeng, Y. R.** and **Tsai, H. J.** Improved model of wafer/pad powder slurry for chemical mechanical polishing. *J. Electrochem. Soc.*, 2003, **150**, G348–G354.
34 **Jeng, Y. R., Huang, P. Y.,** and **Pan, W. C.** Tribological analysis of CMP with partial asperity contact. *J. Electrochem. Soc.*, 2003, **150**, G630–G637.
35 **Tsai, H. J., Jeng, Y. R.,** and **Huang, P. Y.** Elasto-partial hydrodynamic contact model for chemical mechanical polishing. *J. Electrochem. Soc.*, 2006, **153**, G1072–G1077.
36 **Jeng, Y. R.** and **Wang, P. Y.** An elliptical microcontact model considering elastic, elastoplastic and plastic deformation. *Trans. ASME, J. Tribol.*, 2003, **125**, 232–240.
37 **Zhao, Y., McCool, D.,** and **Cheng, L.** An asperity microcontact model incorporating the transition from elastic deformation to fully plastic flow. *ASME J. Tribol.*, 2000, **122**, 86–93.
38 **Jeng, Y. R.** and **Huang, P. Y.** A material removal rate model considering interfacial micro-contact wear behavior for chemical mechanical polishing. *Trans. ASME, J. Tribol.*, 2005, **127**, 190–197.
39 **Abbott, E. J.** and **Firestone, F. A.** Specifying surface quality – a method based on accurate measurement and comparison. *Proc. Instn Mech. Engrs*, 1933, **55**, 569–572.



Downloaded from pij.sagepub.com at PENNSYLVANIA STATE UNIV on September 17, 2016

40 **Johnson, K. L.** *Contact mechanics*, 1985 (Cambridge University Press, Cambridge).
41 **Jeng, Y. R.** and **Tsai, H. J.** Tribological analysis on powder slurry in chemical mechanical polishing. *J. Phys. D, Appl. Phys.*, 2002, **35**, 1585–1591.

## APPENDIX

### Notation

| | |
|---|---|
| $a$ | dimensionless constant |
| $A_n$ | nominal area of contact between two surfaces |
| $d$ | average particle diameter |
| $e$ | coefficient of restitution |
| $f$ | grain size coefficients |
| $g$ | grain size coefficients |
| $h$ | local film thickness |
| $\overline{h}$ | average film thickness |
| $H_S$ | film thickness ratio, $\overline{h}/\sigma$ |
| $H_P$ | film particle ratio, $\overline{h}/d$ |
| $I$ | rate of energy loss due to inelastic collision |
| $k$ | dimensionless constant |
| $K$ | thermal diffusivity coefficient |
| $m$ | average mass of grain particle |
| $p$ | pressure |
| $p_0$ | ambient pressure |
| $R$ | average radius of asperity curvatures |
| $R_1, R_2$ | dimensionless functions |
| $s$ | separation distance between particle surfaces |
| $t$ | dimensionless constant |
| $u$ | macroscopic flow velocity $(u_x, u_y, u_z)$ |
| $u_1, u_2$ | translational velocity of lower and upper surfaces |
| $U_i$ | mean velocity of the two surfaces in $i$th direction |
| $v$ | granular pseudo-temperature (average fluctuation velocity) |
| $V_i$ | slip velocity of the two surfaces along $i$th direction |
| $w$ | dimensionless constant, $1 - e^2$ |
| $x$ | position coordinate $(x, y, z)$ |
| $X, Y$ | transformed coordinate |
| $Z$ | mean surface height, $(z_1 + z_2)/2$ |
| $\gamma$ | Peklenik number |
| $\delta_1, \delta_2$ | random variables of heights of surfaces |
| $\eta$ | viscosity |
| $\eta_a$ | area density of asperities |
| $\theta$ | roughness orientation angle |
| $\rho$ | bulk density |
| $\sigma$ | standard deviation of combined roughness $\delta = \sqrt{\sigma_1^2 + \sigma_2^2}$ |
| $\sigma_1, \sigma_2$ | standard deviation of $\delta_1, \delta_2$ |
| $\varphi(z)$ | distribution function of the asperity heights |
| $\overline{\Phi}_{fs}, \overline{\Phi}_{fp}$ | shear stress factors |
| $\overline{\Phi}_{xx}^{P}, \overline{\Phi}_{xy}^{P}$ | pressure and cross pressure flow factors |
| $\overline{\Phi}_{xx}^{S}, \overline{\Phi}_{xy}^{S}$ | shear and cross shear flow factors |
| $\Psi(H_P)$ | grain flow function |
| $\Omega_i, \Psi_i$ | orientation coefficients of the $i$th surface |



Downloaded from pij.sagepub.com at PENNSYLVANIA STATE UNIV on September 17, 2016